INVERSION OF COMPLEX BODY WAVES—III

By Masayuki Kikuchi and Hiroo Kanamori

ABSTRACT

We have developed a method that inverts seismic body waves to determine the mechanism and rupture pattern of earthquakes. The rupture pattern is represented as a sequence of subevents distributed on the fault plane. This method is an extension of our earlier method in which the subevent mechanisms were fixed. In the new method, the subevent mechanisms are determined from the data and are allowed to vary during the sequence. When subevent mechanisms are allowed to vary, however, the inversion often becomes unstable because of the complex trade-offs between the mechanism, the timing, and the location of the subevents. Many different subevent sequences can explain the same data equally well, and it is important to determine the range of allowable solutions. Some constraints must be imposed on the solution to stabilize the inversion. We have developed a procedure to explore the range of allowable solutions and appropriate constraints. In this procedure, a network of grid points is constructed on the $\tau - l$ plane, where τ and l are, respectively, the onset time and the distance from the epicenter of a subevent; the best-fit subevent is determined at all grid points. Then the correlation is computed between the synthetic waveform for each subevent and the observed waveform. The correlation as a function of τ and l and the best-fit mechanisms computed at each $\tau - l$ grid point depict the character of allowable solutions and facilitate a decision on the appropriate constraints to be imposed on the solution. The method is illustrated using the data for the 1976 Guatemala earthquake.

INTRODUCTION

Seismic body waves are extensively used to determine the rupture pattern of earthquakes. The rupture patterns are generally very complex, and the results are interpreted in terms of a distribution of "asperities" and "barriers" on the fault plane. The rupture pattern is important for an understanding of the mechanism of rupture initiation and termination and excitation of strong ground motions. Many methods have been used to determine the pattern of asperity distributions from seismic waveform data (e.g., Hartzell and Heaton, 1983; Ruff and Kanamori, 1983; Mori and Shimazaki, 1984; Kikuchi and Fukao, 1985).

In the method we have previously presented (Kikuchi and Kanamori, 1982, 1986), the rupture sequence is represented by a sequence of subevents distributed on the fault plane. We assumed that all the subevents have the same mechanism, usually determined from the first-motion data. In some cases, a few subevents were allowed to have a different mechanism. This assumption was made to reduce the number of free parameters and stabilize the inversion. In this paper, we remove this limitation and extend the method to a more general case where subevents are allowed to have different mechanisms. Several investigators have developed similar method. For example, in the inversion method of Nábĕlek (1984), the mechanism of subevents is determined by an iterative least-squares method. Barker and Langston (1981, 1982) developed a generalized inverse technique utilizing the moment tensor formalism. Koyama (1987)

inverted teleseismic long-period body waves to a time sequence of moment tensors. Hirata and Kawasaki (1988) analyzed body waves from a deep earthquake and investigated the change in the fault mechanism during the source process.

Once subevents mechanisms are allowed to vary, the inversion often becomes unstable because of the complex trade-offs between the mechanism, the timing, and the location of the subevents. The solution is inevitably nonunique. Many different sequences can explain the same data equally well, and it is often difficult to determine the range of allowable solutions. In some cases, some constraints have to be imposed on the solution to stabilize the inversion; it is then important to know what constraints are reasonable.

We developed a new method to invert body waves to obtain the mechanism and rupture patterns of complex events. In the earlier method, only P waves were used; in the new method, P, SH, SV, and PP phases can be used simultaneously, and a multi-layer structure is used to compute the response of the source, station, and PP bounce point structures. For this computation, we used the Haskell propagator matrix in the way described in Bouchon (1976) and Haskell (1960, 1962).

In this paper, however, we will focus on the procedure to explore the range of allowable solutions and constraints. We will illustrate the method using the data set from the 1976 Guatemala earthquake.

METHOD

We describe a seismic source as a sequence of point sources with various focal mechanisms. As in our earlier papers, we determine the point sources iteratively by matching the observed records with the synthetic ones. We use a moment tensor to describe each point source.

In general a moment tensor $[M_{ij}]$ has 6 independent elements. With a constraint of vanishing trace of $[M_{ij}]$, we obtain a pure-deviatoric moment tensor. With an additional constraint that the determinant of $[M_{ij}]$ is zero, the moment tensor is reduced to a double-couple source. In the following, we first consider general moment tensors, and then double-couple sources.

General Moment-Tensor Sources

We choose the following 6 elementary moment tensors as the basis tensors to represent a seismic source:

$$\mathbf{M}_1 : \begin{bmatrix} 0 & 1 & 0 \\ 1 & 0 & 0 \\ 0 & 0 & 0 \end{bmatrix} ; \mathbf{M}_2 : \begin{bmatrix} 1 & 0 & 0 \\ 0 & -1 & 0 \\ 0 & 0 & 0 \end{bmatrix} ; \mathbf{M}_3 : \begin{bmatrix} 0 & 0 & 0 \\ 0 & 0 & 1 \\ 0 & 1 & 0 \end{bmatrix} ;$$

$$\mathbf{M}_4 : \begin{bmatrix} 0 & 0 & 1 \\ 0 & 0 & 0 \\ 1 & 0 & 0 \end{bmatrix} ; \mathbf{M}_5 : \begin{bmatrix} -1 & 0 & 0 \\ 0 & 0 & 0 \\ 0 & 0 & 1 \end{bmatrix} ; \mathbf{M}_6 : \begin{bmatrix} 1 & 0 & 0 \\ 0 & 1 & 0 \\ 0 & 0 & 1 \end{bmatrix} ;$$

where the coordinates (x, y, z) for M_{ij} corresponds to (north, east, down). Any moment tensor can be represented by a linear combination of $\mathbf{M}_n$. Figure 1 shows the mechanism diagrams for these elementary tensors. The equal-area projection of the lower focal hemisphere is shown.
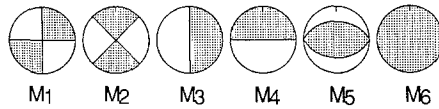
FIG. 1. Elementary moment tensors for the base system used in the inversion (equal-area projection of the lower focal hemisphere).

The advantage of this system is that subgroups of this system represent the specific solutions given below:

(1) $\mathbf{M}_1, \cdots, \mathbf{M}_6$ = general moment tensor,
(2) $\mathbf{M}_1, \cdots, \mathbf{M}_5$ = pure-deviatoric moment tensor,
(3) $\mathbf{M}_1, \cdots, \mathbf{M}_5$ with zero det $[M_{ij}]$ = general double couple,
(4) $\mathbf{M}_1, \cdots, \mathbf{M}_4$ with zero det $[M_{ij}]$ = double couple with a vertical nodal plane,
(5) $M_1, \cdots, \mathbf{M}_2$ = pure strike-slip.

Let $w_{jn}(t; p)$ denote the synthetic seismogram (Green's function) at station j due to nth elementary tensor: $\mathbf{M}_n$, where p is a parameter that collectively represents the onset time, the location, and any other attributes of the source. Denoting the observed seismogram by $x_j(t)$ the best estimate of the coefficient a_n for $\mathbf{M}_n$ can be obtained from

$$
\Delta = \sum_{j=1}^{N_s} \int \left[x_j(t) - \sum_{n=1}^{N_b} a_n w_{jn}(t; p) \right]^2 dt
$$

$$
= R_x - 2 \sum_{n=1}^{N_b} a_n G_n + \sum_{m=1}^{N_b} \sum_{n=1}^{N_b} R_{nm} a_n a_m
$$

$$
= \text{minimum}, \tag{1}
$$

where N_b is the number of the elementary tensors used, N_s is the number of stations, and

$$
R_x = \sum_j \int \left[x_j(t) \right]^2 dt,
$$

$$
R_{nm}(p) = \sum_j \int \left[w_{jn}(t; p) w_{jm}(t; p) \right] dt,
$$

$$
G_n(p) = \sum_j \int \left[w_{jn}(t; p) x_j(t) \right] dt. \tag{2}
$$

Setting

$$
\frac{\partial \Delta}{\partial a_n} = 0; \text{ for } n = 1, \cdots, N_b,
$$

we obtain the normal equation

$$
\sum_{m=1}^{N_b} R_{nm} a_m = G_n, \quad n = 1, \cdots, N_b. \tag{3}
$$

Let the inverse of the matrix $[R_{nm}]$ be $[R^I_{nm}]$, i.e.,

$$\sum_l R_{nl} R^I_{lm} = \delta_{nm}, \; n, \, m = 1, \cdots, N_b,$$

where δ_{nm} is the Kronecker delta. Then the solution is

$$a_n = a^0_n \equiv \sum_m R^I_{nm} G_m. \tag{4}$$

The residual error is then

$$\Delta = R_x - \sum_n G_n a^0_n. \tag{5}$$

At this stage, a^0_n and therefore Δ are functions of the parameter p. The optimum p is determined from the criterion of "minimum Δ," or

$$\Psi_M(p) = \frac{\sum_n G_n a^0_n}{R_x} = \frac{\sum_n \sum_m R^I_{nm} G_m G_n}{R_x}$$

$$= \text{maximum}. \tag{6}$$

Ψ_M is the correlation between the observed and synthetic waveforms. The normalization factor R_x is introduced so that $\Psi_M = 1$, when the observed and synthetic waveforms are identical. Once the optimal p is determined, the values of $\{a^0_n\}$ are given by relation (4). Note that the extent of summations for n and m are set at $N_b = 2, 3, 5, 6$ according to the constraints on the focal mechanism of subevents; hence, a^0_1, a^0_2 for $N_b = 2$ are not identical to a^0_1, a^0_2 of $\{a^0_n\}$ for $N_b > 2$.

Using the coefficients $\{a_n\}$, the resultant moment tensor is given by

$$[M_{ij}] = \begin{bmatrix} a_2 - a_5 + a_6 & a_1 & a_4 \\ a_1 & -a_2 + a_6 & a_3 \\ a_4 & a_3 & a_5 + a_6 \end{bmatrix}.$$

Double-Couple Sources

A moment tensor with zero trace and zero determinant represents a double-couple mechanism. Thus we can find the best-fit double-couple source by imposing the constraint

$$D \equiv \det[M_{ij}] = 0 \tag{7}$$

on a pure-deviatoric moment tensor: $[M_{ij}] = a_1 \mathbf{M}_1 + \cdots + a_5 \mathbf{M}_5$. Let λ be the Lagrangian multiplier, and we minimize the object function

$$\Delta' = \Delta + 2\lambda D \tag{8}$$

with respect to $\{a_n\}$ and λ. Thus, from

$$\frac{\partial \Delta'}{\partial a_n} = \frac{\partial \Delta'}{\partial \lambda} = 0,$$

we find the following equations:

$$a_n = a_n^0 - \lambda \sum_m R^I{}_{nm} \frac{\partial D}{\partial a_m} \tag{9a}$$

and

$$D = 0, \tag{9b}$$

where $\{a_n^0\}$ is the moment-tensor solution given by (4). Equations (9a) and (9b) can be solved numerically. Note that, although D in (9b) does not explicitly include λ, it is cubic with respect to λ through (9a) and equation (9b) has at least one real root for given $\{a_n\}$.

The residual error Δ is given by

$$\Delta = R_x - 2 \sum_n a_n G_n + \sum_m \sum_n R_{nm} a_n a_m$$
$$= R_x - \sum_n \sum_m R_{nm} \big[a_n^0 a_m^0 - \Delta a_n \Delta a_m \big], \tag{10}$$

where $\Delta a_n = a_n - a_n^0$. The correlation between the observed and synthetic waveforms is now given as follows:

$$\Psi_D(p) = \frac{\sum_n \sum_m R_{nm} \big[a_n^0 a_m^0 - \Delta a_n \Delta a_m \big]}{R_x}. \tag{11}$$

Comparing Ψ_D with Ψ_M, we easily find that

$$\Psi_D - \Psi_M = - \frac{\sum_n \sum_m R_{nm} \Delta a_n \Delta a_m}{R_x} < 0,$$

because of the additional constraint imposed on the double-couple solution.

For a single definite focal mechanism, i.e., a definite set of basis tensors, the correlation function between the observed and synthetic waveform is given as follows:

$$\Psi_S = \frac{G_0 a_0}{R_x} = \frac{G_0^2}{R_{00} R_x}, \tag{12}$$

where R_{00} is the auto-correlation of the Green's function, G_0 the cross correlation between the observed and the Green's functions, and

$$a_0 = G_0 / R_{00}. \tag{13}$$

Inversion Procedure

As in our earlier papers, we use an iterative technique to determine subevents from the observed waveforms. The subevents are successively determined by minimizing the squared difference between the observed and synthetic

waveforms with a grid-search over all the values of p. In general, the subevents are determined in the order of decreasing scalar moment (Kikuchi and Kanamori, 1982). The main difference is that the mechanisms of the subevents are determined by the inversion in the present method, while they are fixed in the previous methods.

Allowing the mechanisms of the subevents to vary during the iteration causes a trade-off between the mechanism of a subevent and its onset time. Qualitatively, this trade-off arises from the fact that, for band-limited instruments, a synthetic waveform for a subevent is approximately a sinusoid with the dominant period of the instrument, which is usually 10 to 20 sec. This sinusoid can be matched either by a subevent at the onset of the sinusoid or by a subevent with a reversed polarity shifted in time by half the period. If the record is broadband, this trade-off is less serious. In order to minimize this trade-off, some constraints must be imposed on the solution on the basis of other geological or seismological considerations.

Another problem is that the final solution depends on the order in which the subevents are determined. Young *et al.* (1989) pointed out this problem and called it the path dependence. Thus changing the order of iteration results in different sequences of subevents. It is difficult to decide which sequence is the correct one on the basis of waveform matching alone. In order to see the effect of iteration order on the solution, we introduce an additional procedure after ordinary forward iterations as follows.

After a solution has been obtained with N_e iterations (i.e., N_e subevents), (1) remove subevent 1: (a_{n1}, p_1) and restore its contribution to the seismograms:

$$x'_j(t) = x_j(t) + \sum_n a_{n1} w_{jn}(t; p_1);$$

(2) redetermine subevent 1: $(\hat{a}_{n1}, \hat{p}_1)$ that minimizes

$$\Delta = \sum_{j=1}^{N_s} \int \left[x'_j(t) - \sum_n \hat{a}_{n1} w_{jn}(t; \hat{p}_1) \right]^2 dt.$$

Repeat (1) and (2) for subevents 2 to N_e successively. In effect, this procedure redetermines the parameters of all the subevents by relaxing the constraints imposed by the particular path followed by the first forward iteration.

This procedure always yields a set of N_e subevents that fits the data better. It should be noted, however, that the present inverse problem is nonlinear and non-Gaussian in the sense that there are many local minima of error Δ with respect to source parameters such as the timing and location. The path dependence of the solution is inevitable in any iterative method for non-Gaussian problems. There is no absolute criterion for choosing one solution against the others. The only way is to try iterations for many different paths and choose the solution that is consistent with other data.

Considering the trade-offs between the mechanism and the subevent timing and the path dependence, it is useful to examine the data, before inversion, to get some idea about the overall character of the allowable solution. We use the following procedure to do this. We first compute the correlation function (6 or 11) for the first event. This correlation function is plotted on the $\tau - l$ plane, where τ and l are, respectively, the time lag and the distance of the subevent

from the epicenter. Simple earthquakes may have only one peak, but complex ones yield many peaks. A subevent located at the peak explains the data best. However, because of the trade-off between the mechanism and timing discussed above, subevents with different mechanisms may explain the data equally well if they are slightly displaced from the peak. To see this trade-off, we construct a grid network on the $\tau - l$ plane, place subevents on the grid points, and determine their mechanisms. Comparing these mechanisms with the correlation function Ψ on the $\tau - l$ diagram, we can have an overall picture of the possible range of solutions and guess the type of solutions under different constraints. We will illustrate this procedure for the Guatemala earthquake.

ANALYSIS OF THE 1976 GUATEMALA EARTHQUAKE

The Guatemala earthquake of 4 February 1976 ($M_s = 7.5$) is one of the largest shallow earthquakes occurring on a transform fault. A fault offset with the average of 1 meter was observed along a 200-km-long curved section of the Motagua fault (Plafker, 1976).

Kanamori and Stewart (1978) analyzed teleseismic P waves and suggested that the earthquake consisted of about 10 subevents during the first 2 min. Kikuchi and Kanamori (1982) applied their first version of the inversion method to this event and identified 5 discrete subevents with the same focal mechanisms. Recently Young et al. (1989) used a dataset that includes PP waves, with much better azimuthal coverage of stations, and characterized this earthquake with an asymmetric bilateral rupture along a composite fault plane. They suggested that dip-slip mechanisms are necessary to explain the data satisfactorily.

We chose this event to illustrate the method because it is one of the most complex events, and the difficulties and the problems with this type of inversion have been amply demonstrated by the previous investigators (Kikuchi and Kanamori, 1982; Young et al., 1989).

Data

We used P-wave records observed at 14 WWSSN stations with the epicentral distance between 35° and 90° and PP records at 5 stations at about 120°. These records were digitized and interpolated at a sampling interval of 0.5 sec. To determine the arrival time, we used the ISC Bulletin for P waves and the Jeffreys-Bullen (1958) table for PP waves. Records with a duration of 130 sec after the P or PP arrival time were used in the analysis. The station parameters are listed in Table 1. For epicentral distances less than about 50°, the P-wave record within this time interval is contaminated by PP arrival. Thus, we truncated the waveforms at LPB, MSO, and COR. We also restricted the time window for which the subevents are to be determined to 90 sec from the beginning of the P wave.

Station Weighting

Both the observed records and synthetic Green's functions for all the stations were equalized to WWSSN seismograms with the same gain. Then, considering the azimuthal coverage and the quality of the observed records, we applied station weighting factors as given in Table 1 to both the observed and synthetic waveforms. We did not include PP waves in the inversion, but showed their comparisons with the synthetic waveforms.

TABLE 1

List of Station Parameters

Station	$\Delta(°)$	$\phi(°)$	$\phi_b(°)$	Phase	Comp	Weight
KBS	787.1	11.1	−76.1	P	EW	0.5
KEV	84.3	18.2	−60.4	P	UD	0.5
KTG	68.1	19.5	−106.5	P	UD	0.5
UME	84.6	24.7	−66.0	P	EW	0.5
NUR	87.9	26.8	−62.0	P	UD	0.5
COP	83.8	33.7	−71.8	P	UD	0.5
ESK	75.3	35.9	−84.3	P	UD	0.5
STU	84.0	41.0	−73.7	P	UD	0.5
LPB	38.0	145.8	−34.4	P	EW	1.0
LPA	58.3	149.9	−36.1	P	UD	1.0
RAR	78.2	−116.1	68.3	P	UD	1.0
COR	41.0	−37.4	124.7	P	UD	1.0
MSO	35.7	−27.2	141.0	P	NS	1.0
COL	63.1	−23.9	112.7	P	UD	1.0
PRE	120.9	111.2	−87.0	PP	UD	0.0
GRM	119.6	119.9	−90.6	PP	UD	0.0
RIV	123.0	−120.7	93.2	PP	UD	0.0
RAB	118.8	−86.3	74.8	PP	UD	0.0
TAU	124.8	−132.0	101.9	PP	UD	0.0

Grid Scheme

For the locations of subevents, we took 9 discrete points along the curved Motagua fault at an equal spacing of 30 km and three discrete depths; 7.5, 10.0, and 12.5 km (Figure 2).

Green's Functions

We computed Green's functions for the six elementary moment tensors that are placed at the three discrete depths beneath the epicenter. Green's functions for other grid points can be obtained from these simply by correcting for the differences in travel time. Table 2 gives the structures near the source and the receiver points as well as the bounce point of PP waves. We used Q-filters with the attenuation time constant of $t^* = 1$ sec and convolved a trapezoidal source time function, with $\tau_1 = 5$ and $\tau_2 = 7$ sec, which were found to be the best of several combinations of τ_1 and τ_2 (τ_1 is the rise time and τ_2 is the rise time plus the duration of the top flat portion). The source and receiver functions were computed using the Haskell propagator matrix.

Trade-off between Timing and Mechanism

The nonlinear model parameter p used in the previous section represents the timing τ, the location l along the strike, and the depth h. Figure 3a shows the contour map of the correlation function $\Psi_D(\tau, l, h = 7.5$ km$)$ in the base system of double-couple (equation 11), plotted on the $\tau - l$ plane. Here the set of five pure-deviatoric moment tensors is used as the base system ($N_b = 5$). The solid step-ladder pattern in Figure 3a represents the rupture front with a rupture velocity of 3 km/sec. We assume that no subevents are located on the $\tau - l$ plane behind the rupture front. On the $\tau - l$ plane, there are many peaks that are not clearly isolated, suggesting that many possible combinations of subevents
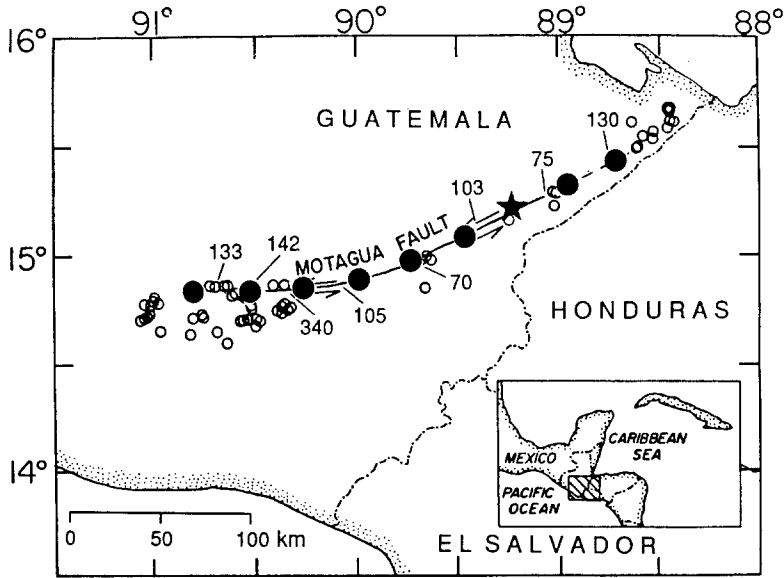
FIG. 2. Grid scheme for discrete source locations (the base figure is taken from figure 1 of Young *et al.*, (1989).

TABLE 2

STRUCTURES

	α (km/s)	β (km/sec)	ρ (g/cm^3)	H (km)
Source and Receiver Structures	6.00	3.50	2.7	18
	6.75	3.80	2.8	18
	8.10	4.70	3.3	
Structure at Bounce Point for *PP* waves	1.50	0.0	1.0	4
	6.00	3.50	2.7	

can explain the data well. The contour pattern for $\Psi_M(\tau, l, h = 7.5$ km) defined by (6) is nearly the same as that shown in Figure 3a.

Figure 3b shows the best-fit double couples placed at grid points 30 km apart in space and 10 sec in time on the $\tau - l$ plane. The regions behind the rupture front are excluded. The trade-off between the timing and the focal mechanism of subevents is clearly displayed. For the first 50 sec, the polarity of the strike-slip mechanism flips alternatingly at every 10 sec. Figures 3c and d show similar diagrams for a different source depth: $h = 12.5$ km. The basic patterns are nearly the same as those of Figures 3a and b, indicating a poor resolution for the source depth. From these diagrams, we can roughly visualize the overall feature of the possible subevent sequence to be obtainable by the inversion. Salient features are the following. (1) Strike-slip sources are predominant during the first 50 sec. (2) Dip-slip sources appear in the later stage of faulting near the western end of the fault. (3) The focal mechanism trades off with the onset time. A time shift of about 10 sec, nearly one half of the predominant period of the observed waveforms, often results in reversal of the focal mechanism.
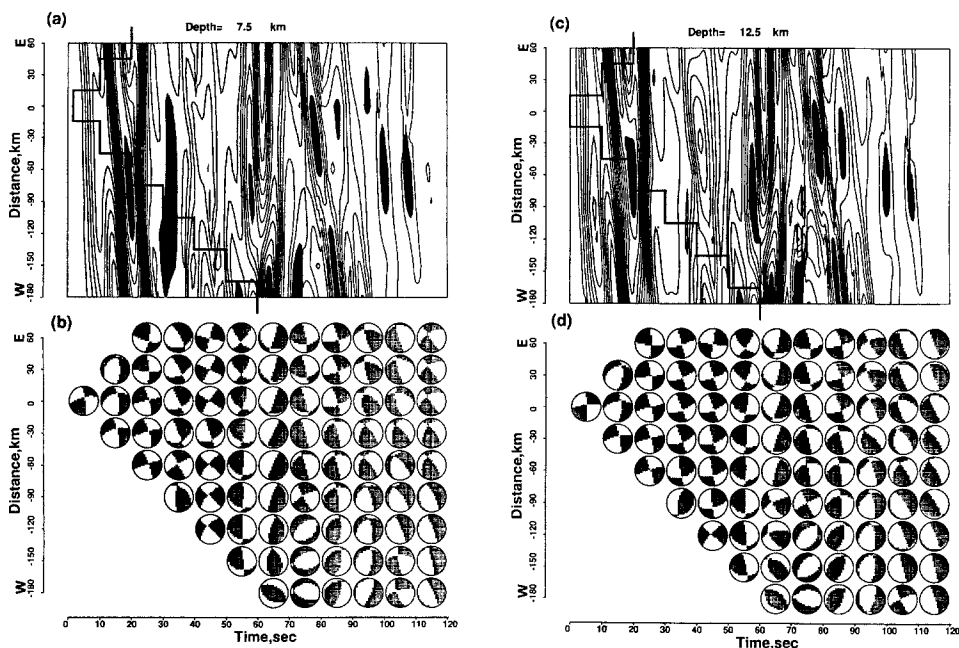
FIG. 3. (a) Contour map of the correlation function Ψ_D computed for a source at the source depth of 7.5 km. Dark zones indicate local maxima of correlation. (b) Mechanism diagrams of the best-fit double couples at grid points at intervals of 30 km and 10 sec on the $\tau - l$ plane. (c) Same as (a) for a source depth of 12.5 km. (d) Same as (b) for a source depth of 12.5 km.

In order to see if dip-slip sources are really needed to model the observed waveforms, we computed the correlation function using the base system of pure strike-slip mechanisms ($N_b = 2$). The contour lines of $\Psi_M(\tau, l, h = 7.5$ km$)$ and the corresponding mechanism disgrams are shown in Figure 4. Strike-slip mechanisms similar to the first-motion mechanism are seen at the western end. However, as we will show later, these subevents alone cannot explain the observed waveforms satisfactorily, suggesting that dip-slip sources are necessary.

Constraints on the Mechanism

The correlation function $\Psi(\tau, l, h)$ exhibits many maxima even for a single subevent. This suggests that many combinations of subevents can fit the data equally well. We need to constrain some of the parameters to obtain a reasonable solution. The effect of such constraints can be demonstrated by the results of our earlier inversion with a fixed mechanism (Kikuchi and Kanamori, 1982). Figure 5 shows the contour lines of $\Psi_S(\tau, l, h = 7.5$ km$)$ where the mechanism is fixed to be the same as the first motion solution $(\phi_s, \delta_s, \lambda_s) = (66°, 90°, 5°)$, (equation 12) where ϕ_s, δ_s, and λ_s are the fault strike, dip, and rake, respectively. Comparing this with the correlation function in Figure 3, we see that the peaks are clearly isolated; the subevents can be identified more uniquely.

In order to avoid the instability caused by the trade-offs displayed in Figures 3b and d, we impose some constraints on the solution. Since the mechanisms opposite to the first-motion mechanism are very unlikely, we constrain the tensile axis of the moment tensors to be within a certain range around that of
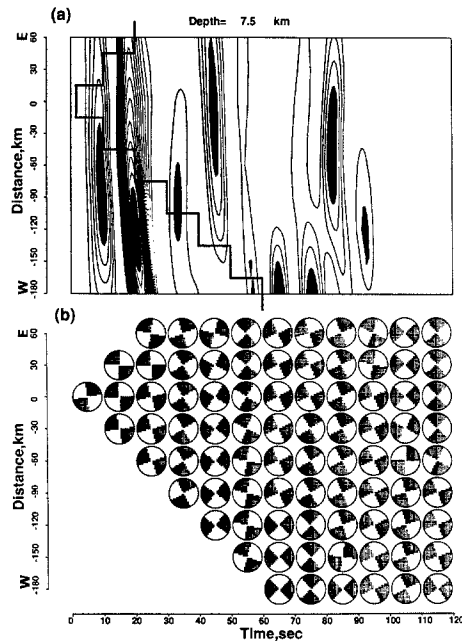
FIG. 4. (a) Contour map of the correlation function Ψ_M computed for a source at the source depth of 7.5 km using the base system of pure strike-slip elements. Peaks of the correlation function are darkened. (b) Mechanism diagrams of the best-fit strike-slip subevents at each grid point at invervals of 30 km and 10 sec.

the first-motion mechanism. In the following examples, we set the allowable range to be from N75°E to N135°E.

Results

First we inverted the data with only pure strike-slip sources (sub group 5). The number of iterations is somewhat arbitrary. We made nine iterations; the waveform match was not significantly improved after the seventh iteration. The results are shown in Figure 6, and the source parameters are listed in Table 3. The total seismic moment is 2.9×10^{27} dyn-cm, which is slightly larger than that obtained from the surface-wave analysis, 2.6×10^{27} dyn-cm (Kanamori and Stewart, 1978). The waveform match is good in the early part but deteriorates after 1 min (Fig. 6c). In particular, the amplitude of the synthetic waveform is too small for RAR. The final residual error Δ is 0.64, which is much larger than that for other solutions described later. Thus, strike-slip mechanisms alone cannot model the rupture process of this earthquake.

Next we performed an inversion with double-couple sources, which allows both strike-slip and dip-slip mechanisms. The main features of the observed waveforms could be satisfactorily reproduced with nine subevents. The residual error Δ is 0.42. After the forward iteration, we repeated twice the redetermination procedure described in the previous section. This procedure reduced Δ to 0.39. The final solution is shown in Figure 7. Table 4 gives the source parameters for the final solution. In Figure 8, the synthetic waveforms are compared with the observed ones. Note that the waveform match is good even for *PP* records, which are not used in the inversion.
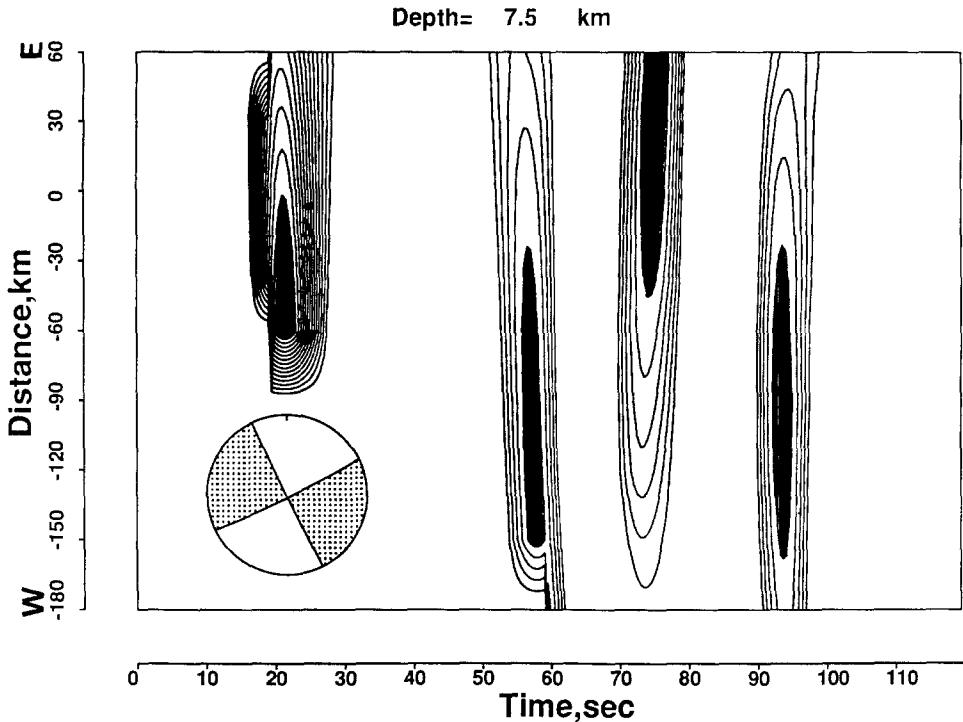
FIG. 5. Contour map of the correlation function Ψ_S computed for a source at the source depth of 7.5 km. The mechanism of the subevent is fixed to be the first-motion solution.

The results may be summarized as follows.

(1) Rupture propagation is mostly unilateral to the west.

(2) A strike-slip mechanism is predominant in the moment release.

(3) The gradual change in the fault strike with the distance from the initial break is not obvious in the result.

(4) Dip-slip subevents occur near both ends of the fault: a normal dip slip near the epicenter with a moment of 1.5×10^{25} dyn-cm, and a reverse dip slip at the western end with a moment of 1.1×10^{26} dyn-cm. Their contribution to the observed P and PP waves is comparable to that from the strike-slip subevents, although the moments of the dip-slip events are much smaller, only 10% in total.

(5) The tensorial sum of all the subevent mechanisms is essentially strike-slip with a small nondouble couple component $(< 3\%)$ and a scalar moment of 2.1×10^{27} dyn-cm, which is slightly smaller than that obtained from surface waves.

A large strike-slip event was obtained at 60 km west of the epicenter about 20 sec after the origin time. Considering the spatial resolution of about 30 km as inferred from the contour lines of $\Psi_D(\tau, l)$ in Figure 3a, the location of this subevent can be close to the bend of the Motagua fault. This subevent coincides with the largest subevent identified by Young et al. (1989).

DISCUSSION

If the mechanisms of the subevents are allowed to vary and if no constraints are imposed on them, the inversion becomes unstable. Many different combina-
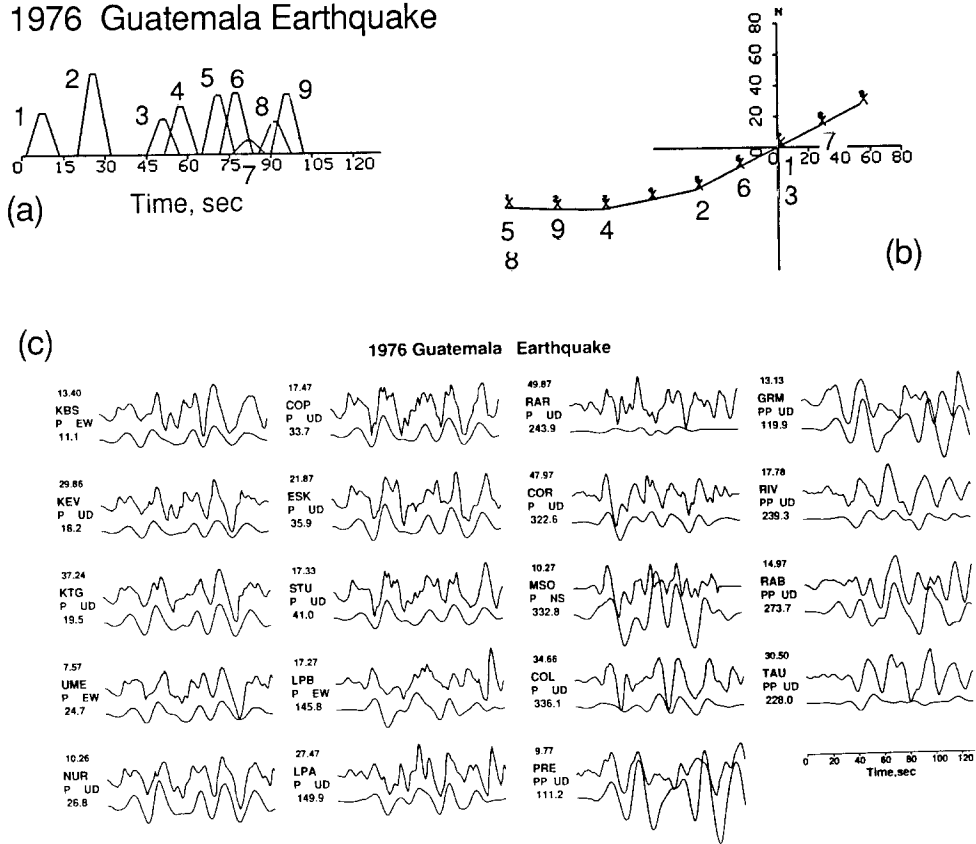
1976 Guatemala Earthquake

(a) Time, sec

(b)

(c)

1976 Guatemala Earthquake

FIG. 6. Results of the inversion with pure strike-slip sources. The azimuth of the T axis is constrained to be between N75°E and N135°E. (a) Time sequence of subevents; (b) location of subevents; (c) examples of observed (upper) and synthetic (lower) waveform. The numbers on the *upper* and *lower left* indicate the peak-to-peak amplitude in micrometers of the observed record and the azimuth, respectively. The synthetic records are plotted with the same scale as the observed.

TABLE 3

RESULTS OF THE INVERSION WITH PURE STRIKE SLIPS

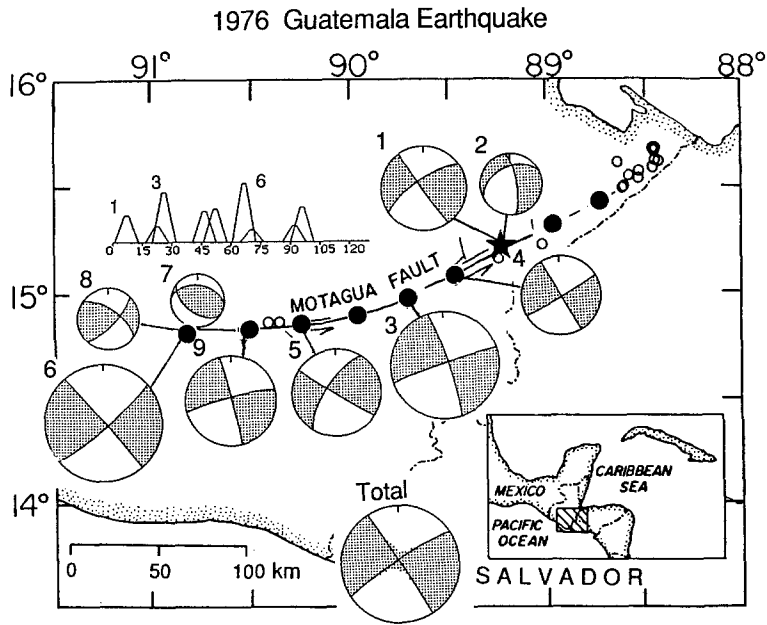| Onset (sec)	Distance (km)	Depth (+10.0 km)	Moment ($\times 10^{25}$ dyn.cm)	Strike (°)	Dip (°)	Slip (°)
1.5	−0.0	0.0	31.7	57.0	90.0	0.0
20.0	−60.0	−2.5	60.9	71.5	90.0	0.0
45.0	−0.0	−5.0	26.6	31.3	90.0	0.0
51.5	−120.0	−5.0	35.5	52.0	90.0	0.0
65.0	−180.0	−5.0	44.1	42.6	90.0	0.0
71.5	−30.0	0.0	45.3	61.7	90.0	0.0
76.0	30.0	−5.0	9.9	86.9	90.0	0.0
85.5	−180.0	−5.0	23.8	39.2	90.0	0.0
90.0	−150.0	0.0	45.3	61.7	90.0	0.0
			286.9	56.6	90.0	0.0

Residual error $\Delta = 0.636$.

FIG. 7. Final results of the inversion. Time sequence and location of subevents are shown. The area of the mechanism diagrams is proportional to the seismic moment.

TABLE 4

SOURCE PARAMETERS FOR THE FINAL SOLUTION

Onset (sec)	Distance (km)	Depth (+12.5 km)	Moment ($\times 10^{25}$ dyn.cm)	Strike (°)	Dip (°)	Slip (°)
1.0	0.0	0.0	24.9	63.1	86.9	-0.6
16.5	0.0	-5.0	14.9	353.3	75.0	-130.1
20.0	-60.0	0.0	46.2	73.5	86.9	6.2
40.5	-30.0	0.0	28.5	144.8	86.5	162.7
46.0	-120.0	-5.0	30.6	123.5	87.1	160.5
60.5	-180.0	0.0	54.4	48.9	82.7	1.9
64.5	-180.0	2.5	11.1	127.4	51.6	108.9
86.0	-180.0	-2.5	15.0	35.0	69.2	25.4
90.0	-150.0	0.0	32.2	346.1	87.3	-173.3
			212.8	328.8	88.4	-173.4

Residual error $\Delta = 0.388$.

tions of the model parameters, such as the timing and the location of subevents, yield many local minima of the approximation error. The problem is nonlinear and nonunique; we cannot determine "the best" solution from the waveform inversion alone.

Under these circumstances, it is essential to first investigate the gross features of all the possible solutions. It is also important to inspect possible trade-offs between the model parameters. Through this inspection, we can introduce appropriate constraints to be imposed on the solution to stabilize the inversion. The correlation function $\Psi(p)$ (6 or 11) combined with the mechanism diagrams on the $\tau - l$ plane is useful for this purpose. In the present
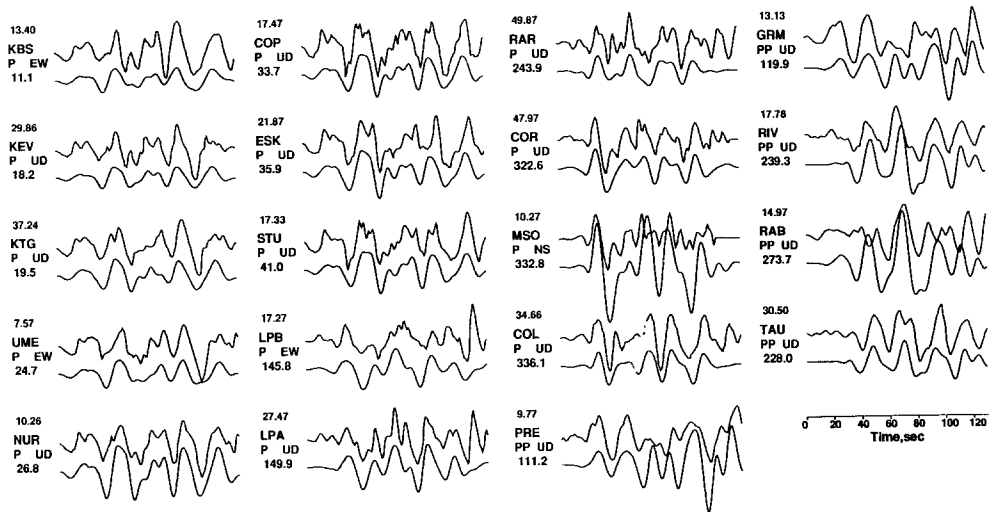
1976 Guatemala Earthquake

FIG. 8. Synthetic waveforms (lower trace) for the final solution shown in Figure 7 compared with the observed ones (upper trace). The amplitude scale is the same as that in Figure 6.

analysis, we constrained the tension axis of the moment tensors. Smoothness constraints may also be useful when the mechanism change is known to be small from other observations.

In analysing body waves from the Guatemala earthquake, we constrained the T axis to be in a certain range. This is only one of the many possible constraints. We need to introduce constraints considering the results from other studies such as long-period surface-wave, geodetic, and geological studies. Our results are consistent with the results from surface-wave analysis and field observations. Dip-slip subevents are necessary to explain some features of the seismograms. Without a dip-slip mechanism, we had to include many strike-slip subevents with a total seismic moment exceeding that determined from surface waves. Subsidiary faults with a predominant dip-slip component are observed near the western end of the Motagua fault (Plafker, 1976).

Most of the faults reported in the field observations are not reverse but normal faults, while our inversion yields both reverse and normal faults.

REFERENCES

Barker, J. and C. A. Langston (1981). Inversion of teleseismic body waves for the moment tensor of the 1978 Thessaloniki, Greece, earthquake, *Bull. Seism. Soc. Am.* **71,** 1423–1444.

Barker, J. and C. A. Langston (1982). Moment tensor inversion of complex earthquakes, *Geophys. J. R. Astr. Soc.* **68,** 777–803.

Bouchon, M. (1976). Teleseismic body wave radiation from a seismic source in a layered medium, *Geophys. J. R. Astr. Soc.* **47,** 515–530.

Hartzell, S. H. and T. H. Heaton (1983). Inversion of strong ground motion and teleseismic waveform data for the fault rupture history of the 1979 Imperial Valley, California, earthquake, *Bull. Seism. Soc. Am.* **73,** 1553–1583.

Haskell, N. A. (1960). Crustal reflection of plane *SH* waves, *J. Geophys. Res.* **65**, 4147–4150.

Haskell, N. A. (1962). Crustal reflection of plane *P* and *SV* waves, *J. Geophys. Res.* **67**, 4751–4767.

Hirata, K. and I. Kawasaki (1988). Space-time dependent moment tensor, *Programme and Abstracts Seism. Soc. Japan*, *No.* 2, **16** (in Japanese).

Jeffreys, H. and K. E. Bullen (1958). *Seismological tables*. Office of the British Association, Burlington House, London.

Kanamori, H. and G. S. Stewart (1978). Seismological aspects of the Guatemala earthquake of February 4, 1976, *J. Geophys. Res.* **83**, 3427–3434.

Kikuchi, M. and Y. Fukao (1985). Iterative deconvolution of complex body waves from great earthquakes; the Tokachi-Oki earthquake of 1968, *Phys. Earth Planet. Interiors* **37**, 235–248.

Kikuchi, M. and H. Kanamori (1982). Inversion of complex body waves, *Bull. Seism. Soc. Am.* **72**, 491–506.

Kikuchi, M. and H. Kanamori (1986). Inversion of complex body waves—II, *Phys. Earth Planet. Interiors*, **43**, 205–222.

Koyama, J. (1987). Time-dependent moment tensor inversion for the 1983 Japan sea earthquake, *Zisin* 2, **40**, 405–416 (in Japanese with English abstract).

Mori, J. and K. Shimazaki (1984). High stress drops of short-period subevents from the 1968 Tokachi-Oki earthquake as observed on strong-motion records, *Bull. Seism. Soc. Am.* **74**, 1529–1544.

Nábĕlek, J. L. (1984). Determination of earthquake source parameters from inversion of body waves, *Ph.D. Thesis*, MIT, Cambridge, Massachusetts.

Plafker, G. (1976). Tectonic aspects of the Guatemala earthquake of 4 February 1976, *Science* **93**, 1201–1208.

Ruff, L. and H. Kanamori (1983). The rupture process and asperity distribution of three great earthquakes from long-period diffracted *P* waves, *Phys. Earth Planet. Interiors* **31**, 202–230.

Young, C. J., T. Lay, and C. S. Lynnes (1989). Rupture of the 4 February 1976 Guatemalan earthquake, *Bull. Seism. Soc. Am.* **79**, 670–689.

SEISMOLOGICAL LABORATORY 252-21   DEPARTMENT OF PHYSICS
CALIFORNIA INSTITUTE OF TECHNOLOGY   YOKOHAMA CITY UNIVERSITY
PASADENA CALIFORNIA 91125   YOKOHAMA 236, JAPAN
    (H.K.)   (M.K.)